

# How to inflate a wind-blown bubble

J. M. Pittard<sup>\*</sup>, C. J. Wareing and M. M. Kupilas

*School of Physics and Astronomy, University of Leeds, Woodhouse Lane, Leeds LS2 9JT, UK*

Accepted 2021 September 13. Received 2021 September 13; in original form 2021 July 30

## ABSTRACT

Stellar winds are one of several ways that massive stars can affect the star formation process on local and galactic scales. In this paper we investigate the numerical resolution needed to inflate an energy-driven stellar wind bubble in an external medium. We find that the radius of the wind injection region,  $r_{\text{inj}}$ , must be below a maximum value,  $r_{\text{inj,max}}$ , in order for a bubble to be produced, but must be significantly below this value if the bubble properties are to closely agree with analytical predictions. The final bubble momentum is within 25 per cent of the value from a higher resolution reference model if  $\chi = r_{\text{inj}}/r_{\text{inj,max}} = 0.1$ . Our work has significance for the amount of radial momentum that a wind-blown bubble can impart to the ambient medium in simulations, and thus on the relative importance of stellar wind feedback.

**Key words:** methods: numerical – ISM: bubbles – stars: massive – stars: winds, outflows – stars: mass-loss – stars: early-type

## 1 INTRODUCTION

Massive stars have dramatic impacts on their surroundings, through their intense radiation, and their powerful winds and supernova explosions. These stellar inputs rapidly destroy the molecular clouds in which stars form, and are also able to affect the global structure and evolution of their host galaxy. The momentum that is injected into the interstellar medium (ISM), plus the boost through  $PdV$  work done by over-pressured expanding gas, determines the amplitude of the turbulent gas motions, which limit gravitational condensation and collapse, and ultimately limit and regulate star formation (e.g., Shetty & Ostriker 2012).

Recent work has indicated that early (pre-supernova) feedback from winds and radiation is required to explain the anti-correlation of giant molecular clouds (GMCs) and ionized regions on 100 pc scales and less (e.g., Kruijssen et al. 2019; Chevance et al. 2020, 2021). GMCs appear to disperse within 1 – 5 Myr of massive stars emerging from their natal clouds, with photoionization and stellar winds seeming to play a crucial role. Cosmological simulations with only supernova (SN) feedback also show that SNe alone are not able to prevent excessive star formation (e.g., Smith, Sijacki & Shen 2019).

Nonetheless, the impact of stellar winds remains much debated. El-Badry et al. (2019) showed that turbulent mixing at the interface between the hot interior gas and colder exterior gas sets the cooling losses, which reduces the radial momentum by a factor of 2. However, the applicability of the classical energy-conserving wind-blown-bubble approach (Weaver et al. 1977) has recently been questioned by Lancaster et al. (2021a,b), who argue that if the interface becomes fractal-like due to the presence of inhomogeneities in the ambient gas, radiative losses can become very substantial and cause the bubble to display momentum-conserving-like behaviour. Dinn-

bier & Walch (2020) argued that stellar winds and photoionization are quenched in clusters with a mass above  $10^4 M_{\odot}$ .

Many works simply assume that the feedback from winds is momentum-driven (e.g., Dale et al. 2014), which sets a lower limit to their impact. On the other hand, if stellar winds couple relatively weakly to the densest clumps of gas in star-cluster environments, the winds can carve and open up low-density channels within their environments (e.g., Rogers & Pittard 2013; Wareing et al. 2017b) and thus are still able to create wind-blown bubbles with low density hot interiors, that might be capable of doing significant  $PdV$  work. Stellar wind feedback may also be shaped by the large scale density distribution arising from a large-scale magnetic field (e.g., Wareing et al. 2017a, 2018) or gas motions.

The significant momentum boost that can be provided by a wind-blown bubble is key to having strong stellar wind feedback. However, to correctly determine the momentum boost requires that simulations have a certain numerical resolution that we find has not always been achieved in the literature. In this work we examine the different ways that a wind can be initiated and also how the development of the wind-blown bubble depends on numerical resolution. We focus only on the effect of the wind, so that other effects due to photoionization, for example, do not complicate the matter. In Sec. 2 we discuss the essential theory of wind-blown bubbles. In Sec. 3 we describe our numerical model and the implementation of the wind driving, and in Secs. 4 and 5 we present and discuss our results. We summarize and conclude in Sec. 6.

## 2 WIND-BLOWN BUBBLES

### 2.1 Essential features

The essential features of an idealised spherically-symmetric wind-blown bubble are (moving outwards from the wind source) an inner region where the wind is freely expanding, a region of shocked wind,

<sup>\*</sup> E-mail: j.m.pittard@leeds.ac.uk

and a region of swept-up ambient material. The shocked and unshocked wind regions are separated by a reverse shock (RS), the wind and ambient gas is separated by a contact discontinuity (CD), and the swept-up material is bounded by a forward shock (FS). Typically, the shocked wind is at much lower density than the ambient gas and remains hot with long cooling timescales, whereas the swept-up gas cools efficiently and is compressed into a cooler shell. The radius of an adiabatic wind-blown bubble (where there is no cooling of the shocked wind) with a thin swept-up shell is (e.g., [Dyson & Williams 1980](#))

$$r_{\text{bub}} = \left( \frac{125}{154\pi} \right)^{1/5} \left( \frac{\dot{E}}{\rho_{\text{amb}}} \right)^{1/5} t^{3/5}, \quad (1)$$

where  $\dot{E}$  is the rate of energy injection of the wind ( $\dot{E} = \frac{1}{2} \dot{M} v_w^2$ , where  $\dot{M}$  is the mass-loss rate of the star and  $v_w$  is the terminal speed of the wind),  $\rho_{\text{amb}}$  is the density of the ambient medium and  $t$  is the bubble age. This equation is valid when the pressure of the bubble is much greater than the pressure of the ambient gas (for solutions when this is not the case see [García-Segura & Franco 1996](#)). We define the radius of the reverse shock and contact discontinuity as  $r_{\text{rs}}$  and  $r_{\text{cd}}$ , respectively.

The bubble is initially of zero size ( $r_{\text{rs}} = r_{\text{cd}} = r_{\text{bub}} = 0$  at  $t = 0$ ). All 3 radii then increase with time. The bubble will expand as long as its interior pressure exceeds the ambient pressure,  $P_{\text{amb}}$ , or as long as the lifetime of the source. The thermal pressure within the bubble is (e.g., [Dyson & Williams 1980](#); [Pittard 2013](#))

$$P_{\text{bub}} = \frac{7}{(3850\pi)^{2/5}} \dot{E}^{2/5} \rho_{\text{amb}}^{3/5} t^{-4/5}. \quad (2)$$

At all times the position of the reverse shock is set by pressure balance between the ram pressure of the hypersonic wind (in the frame of the reverse shock) and the thermal pressure of the hot bubble:

$$\rho_w (v_w - v_{\text{rs}})^2 \approx P_{\text{bub}}, \quad (3)$$

where  $\rho_w$  is the pre-shock density of the wind at the reverse shock and  $v_{\text{rs}}$  is the velocity of the reverse shock. If the radial velocity of the reverse shock is ignored, the reverse shock position is given by

$$r_{\text{rs}} \approx \left( \frac{\dot{M} v_w}{4\pi P_{\text{bub}}} \right)^{1/2} \approx 0.70 (\dot{M} v_w)^{1/2} \dot{E}^{-1/5} \rho_{\text{amb}}^{-3/10} t^{2/5}. \quad (4)$$

The reverse shock will be slightly closer to the star if  $v_{\text{rs}}/v_w$  is significant (e.g., at early times). The reverse shock attains a maximum radius,  $r_{\text{rs,max}}$ , when  $P_{\text{bub}} = P_{\text{amb}}$ . This is given by

$$r_{\text{rs,max}} \approx \left( \frac{\dot{M} v_w}{4\pi P_{\text{amb}}} \right)^{1/2}, \quad (5)$$

and occurs when the bubble age is

$$t_{\text{rs,max}} = 0.104 \dot{E}^{1/2} \rho_{\text{amb}}^{3/4} P_{\text{amb}}^{-5/4}. \quad (6)$$

Given that  $t_{\text{rs,max}}$  may be (much) greater than the lifetime of the star, a more useful measure than  $r_{\text{rs,max}}$  is the radius of the reverse shock at the end of life of the star, which we define to be

$$r_{\text{rs,tlife}} \approx 0.70 (\dot{M} v_w)^{1/2} \dot{E}^{-1/5} \rho_{\text{amb}}^{-3/10} t_{\text{life}}^{2/5}, \quad (7)$$

where  $t_{\text{life}}$  is the lifetime of the star. In fact, unless the wind is very weak and the ambient pressure is very high, we always expect  $t_{\text{life}} < t_{\text{rs,max}}$  (see Sec. 4 for typical values of  $t_{\text{rs,max}}$  and  $t_{\text{life}}$ ).

## 2.2 Momentum injection

The wind injects momentum at a rate  $\dot{p}_{\text{wind}} = \dot{M} v_w$ , so the momentum supplied by the wind,

$$p_{\text{wind}} = \dot{p}_{\text{wind}} t. \quad (8)$$

However, the  $PdV$  work by the bubble on the surrounding gas means that the momentum of the bubble (which is dominated by the swept-up shell) is

$$p_{\text{bub}} = \frac{4\pi}{3} r_{\text{bub}}^3 \rho_{\text{amb}} \dot{r}_{\text{bub}} = 0.85 \dot{E}^{4/5} \rho_{\text{amb}}^{1/5} t^{7/5}. \quad (9)$$

The momentum boost provided by the bubble is

$$\beta = \frac{p_{\text{bub}}}{p_{\text{wind}}} = 0.60 \dot{E}^{3/10} \dot{M}^{-1/2} \rho_{\text{amb}}^{1/5} t^{2/5}. \quad (10)$$

$\beta$  can easily have a value in excess of 100.

Since the wind momentum increases linearly with time, while the wind-blown bubble momentum increases as  $t^{7/5}$ , at early times the wind will have more momentum than the bubble. This non-sensical result indicates a break-down of the bubble model at early times. It arises because the bubble has not existed long enough to have properly developed its characteristic features. We define the time at which  $p_{\text{wind}} = p_{\text{bub}}$  as

$$t_{\text{eq}} = 3.57 \dot{M}^{5/4} \dot{E}^{-3/4} \rho_{\text{amb}}^{-1/2}. \quad (11)$$

## 3 THE NUMERICAL MODEL

There are a number of different ways that a hypersonic stellar wind can be modelled using a grid-based hydrodynamics code. In all cases several cell-averaged quantities inside of a ‘‘remap’’ or ‘‘injection’’ radius,  $r_{\text{inj}}$ , are altered or reset at each timestep,  $dt$ . The volume of the injection region is  $V_{\text{inj}}$ . Typically  $r_{\text{inj}}$  and  $V_{\text{inj}}$  are fixed, but there is no reason why they might not instead be time dependent (e.g., if the grid adaptively derefines or is expanding - as we show later).

In the following we shall assume for simplicity that the wind is spherically symmetric and that it blows into a static medium with a uniform density and pressure (though this is often not the case in reality). We also assume that there is no non-thermal contribution to the ambient pressure. Table 1 notes details of our models and the final momentum and momentum boost that is obtained.

### 3.1 Some possible implementations

#### 3.1.1 Momentum and energy overwrite (method meo)

In this scenario, which is perhaps the simplest approach, the density and velocity of each cell with  $r < r_{\text{inj}}$  are set to values appropriate for a free-flowing wind. In the case of a spherically symmetric wind, if the inner and outer radius of the cell are  $r_i$  and  $r_o$ , respectively, then the mass within the cell is

$$M = \int_{r_i}^{r_o} 4\pi r^2 \rho dr = \frac{\dot{M}}{v_w} (r_o - r_i). \quad (12)$$

Since the volume of the cell is  $\frac{4}{3}\pi(r_o^3 - r_i^3)$ , the cell density

$$\rho = \frac{3\dot{M}}{4\pi v_w} \frac{(r_o - r_i)}{(r_o^3 - r_i^3)}. \quad (13)$$

The cell velocity  $\mathbf{v} = v_w$ . The existing values in each cell are overwritten at each time step and previous information about the flow within the injection region is lost. The pressure in the cell is set so

that the cell temperature is at a desired value (e.g.,  $10^4$  K, or the floor temperature of the simulation,  $T_{\text{floor}}$ ). As long as the sound speed in the wind is much less than the wind speed (i.e. the wind is hypersonic), the exact temperature of the wind will not be important as the kinetic energy dominates. In this procedure the wind energy is almost purely kinetic, and the density within the injection region falls as  $1/r^2$ .

### 3.1.2 Thermal energy injection (method ei)

Another possibility is to inject the wind energy as purely thermal. The mass and energy injection from the wind are shared uniformly for cells with  $r < r_{\text{inj}}$ . The procedure, which is applied to each cell within the injection region at every time step is (Chevalier & Clegg 1985; Wunsch et al. 2008):

- (i) Add mass to the cell:  $\rho_{\text{new}} = \rho_{\text{old}} + d\rho$ , where  $d\rho = \dot{M} dt / V_{\text{inj}}$ .
- (ii) Conserve momentum:  $\mathbf{v}_{\text{new}} = \mathbf{v}_{\text{old}} \rho_{\text{old}} / \rho_{\text{new}}$ .
- (iii) Calculate the new kinetic energy density in the cell and subtract from the old total energy density,  $e_{\text{tot,old}}$ , to give the new internal energy density prior to the addition of the new (thermal) energy:  $e_{\text{int}} = e_{\text{tot,old}} - \rho_{\text{new}} \mathbf{v}_{\text{new}}^2 / 2$ .
- (iv) Add the new (thermal) energy to the new internal energy density:  $e_{\text{int,new}} = e_{\text{int}} + \dot{E} dt / V_{\text{inj}}$ .

In the above prescription, the old and new values in the cell have the subscript “old” and “new”, respectively.

With this procedure the flow is thermally driven, and transitions from subsonic to supersonic at the edge of the injection region. Outside of the injection region the flow continues to accelerate due to the thermal pressure gradient, and asymptotically reaches its terminal speed of  $v_w = \sqrt{2\dot{E}/\dot{M}}$  at large radii. Because cell quantities within the injection region retain some element of their previous values, the resultant flow has some sensitivity to the initial parameters and may develop differently in certain situations. For instance, if the initial gas density within the injection region is very high, rapid cooling of the gas may suppress development of the wind. If cooling is not significant, the temperature of the injection region gradually increases until a stationary flow is produced.

This prescription has the drawback that at early times velocities and temperatures within the injection region may be low. Some additional constraints on  $dt$  other than the dynamics may then be necessary (e.g., a cooling time constraint).

### 3.1.3 Momentum and energy injection (method mei)

Another possibility is to inject mass, momentum and energy evenly into all cells (Geen et al. 2021). The procedure is:

- (i) Add mass to each cell:  $\rho_{\text{new}} = \rho_{\text{old}} + d\rho$ .
- (ii) Add momentum to each cell:  $\mathbf{v}_{\text{new}} = (\rho_{\text{old}} \mathbf{v}_{\text{old}} + d\rho \mathbf{v}_w) / \rho_{\text{new}}$ .
- (iii) Add energy to each cell:  $e_{\text{tot,new}} = e_{\text{int,old}} + 0.5 \rho_{\text{old}} \mathbf{v}_{\text{old}}^2 + de$ , where  $de = 0.5 d\rho v_w^2$ , the old internal energy density is  $e_{\text{int,old}}$ , and  $e_{\text{tot,new}}$  is the new total energy density.
- (iv) Although not explicitly stated by Geen et al. (2021), in order to conserve energy the internal energy density of the cell must become  $e_{\text{int,new}} = e_{\text{tot,new}} - 0.5 \rho_{\text{new}} \mathbf{v}_{\text{new}}^2$ .

In this scenario, the stationary flow develops so that the density and pressure within the injection region increase with radius (in contrast to method *ei* where these quantities decline), and the velocity of gas within the injection region is everywhere equal to the wind speed (like the fixed speed overwrite procedure in Sec. 3.1.1). Like the

method in Sec. 3.1.2, this method has some sensitivity to the initial conditions, but has the potential advantage that it may force shorter dynamical timesteps early in the simulation.

## 3.2 Resolution requirements

In order for the wind to have *any* chance of inflating a bubble using the *meo* wind injection method, the wind ram pressure at the edge of the injection region must exceed the ambient pressure. Alternatively, if the *ei* wind injection method is used, the central pressure in the injection region should exceed  $P_{\text{amb}}$ . Both requirements result in essentially the same maximum size of the injection region,

$$r_{\text{inj,max}} = \left( \frac{\dot{M} v_w}{4\pi P_{\text{amb}}} \right)^{1/2}, \quad (14)$$

above which we do not expect a bubble to be created. We define

$$\chi = \frac{r_{\text{inj}}}{r_{\text{inj,max}}}. \quad (15)$$

Simulations with  $\chi < 1$  should inflate a bubble. However, if this is only marginally satisfied, we do not expect the resulting bubble to match the analytical solution. In such a scenario the bubble would not experience such high initial pressures as seen in better resolved bubbles early in their life - as a result they will evolve to be too small with too little radial momentum.

In order not to miss *any* initial momentum boost with the *meo* injection method, the initial conditions should be set so that the momentum (in the injection region) of the outflowing wind (which has a flow-time or age  $t = r_{\text{inj}}/v_w$ ) is substantially greater than the momentum of a wind-blown bubble of equivalent age (i.e.  $t \ll t_{\text{eq}}$  - see Eq. 11). This sets the constraint  $r_{\text{inj}} \ll v_w t_{\text{eq}}$ . In essence, this requirement ensures that the simulation starts prior to the bubble generating additional momentum through  $PdV$  work.

## 3.3 The calculations

We are investigating the evolution of a wind-blown bubble. It makes sense, therefore, to use a code where the grid can expand with time (if desired). We therefore make use of a heavily modified version of VH-1<sup>1</sup>. The standard inviscid equations of hydrodynamics in conservative lagrangian form are solved on a spherically symmetric one-dimensional grid. Piecewise parabolic spatial reconstruction is used to calculate the interface values. The updated quantities are then remapped to the original (or an expanding) grid at the end of each step (this is the piecewise parabolic method (PPM) with lagrangian remap (“PPMLR”) approach used by VH-1). We use a courant number of 0.6.

Gas can heat and cool via operator splitting. The rate of change of the internal energy per unit volume is given by

$$\dot{e} = n\Gamma - n^2\Lambda, \quad (16)$$

where  $n = \rho/m_{\text{H}}$  and  $\Gamma$  and  $\Lambda$  are heating and cooling coefficients. In this work we assume that  $\Gamma = 2 \times 10^{-26} \text{ erg s}^{-1}$  (independent of  $\rho$  or  $T$ ). The cooling coefficient,  $\Lambda(T)$ , is detailed in Wareing et al. (2016). The low temperature part ( $T \leq 10^4$  K) is a corrected fit to the data in Koyama & Inutsuka (2000). Between  $10^4 - 10^{7.6}$  K cooling rates calculated with CLOUDY v10.00 (Gnat & Ferland 2012) are used, while cooling rates calculated from the MEKAL plasma emission

<sup>1</sup> <http://wonka.physics.ncsu.edu/pub/VH-1/>

code (Kaastra 1992; Mewe et al. 1995, as distributed in XSPEC v11.2.0) are used for  $T \geq 10^{7.6}$  K.

We restrict cooling at unresolved interfaces between hot diffuse gas and cold dense gas by replacing the change in the internal energy density,  $de$ , with the minimum of the neighbouring  $de$ 's at the interface. The cooling is sub-cycled so that the cooling curve is always sampled with a temperature resolution of at least 20 per cent.

We also assume solar abundances for the gas (mass fractions  $X_{\text{H}} = 0.7381$ ,  $X_{\text{He}} = 0.2485$ , and  $X_{\text{Z}} = 0.0134$ ; Grevesse et al. 2010), and a temperature-dependent average particle mass,  $\mu$ , is used. In the molecular phase  $\mu = 2.36$ , reducing to 0.61 in ionized gas. The value of  $\mu$  is determined from a look-up table of values of  $p/\rho$  (Sutherland 2010). A temperature-independent value of  $\gamma$ , the ratio of specific heats, is used, which we set to  $\gamma = 5/3$  (see Krumholz, Stone & Gardiner (2007) for arguments as to why this is also appropriate for low temperature molecular gas).

## 4 RESULTS

In all of our calculations the stellar wind and ambient medium parameters are set to  $\dot{M} = 10^{-7} M_{\odot} \text{ yr}^{-1}$ ,  $v_w = 2000 \text{ km s}^{-1}$ ,  $\rho_{\text{amb}} = 2 \times 10^{-21} \text{ g cm}^{-3}$  and  $P_{\text{amb}} = 1.48 \times 10^{-12} \text{ dyn cm}^{-2}$  ( $P_{\text{amb}}/k = 1.07 \times 10^4 \text{ K cm}^{-3}$ ). These are typical of a massive hot star on the main sequence and the cold molecular medium. However, we expect our results to be applicable to a wide range of wind and ISM parameters, including for example superbubbles. The ambient medium has an equilibrium temperature  $T_{\text{amb}} = 21 \text{ K}$  and average particle mass  $\mu_{\text{amb}} = 2.36$ . The ionized wind material has an average particle mass  $\mu_w = 0.61$ .

Our chosen parameters give  $r_{\text{rs,max}} = 2.8 \text{ pc}$  (Eq. 5) at  $t_{\text{rs,max}} = 215 \text{ Myr}$ . However, we only evolve the simulations for 5 Myr, this being more typical of the lifetime of a massive star with the adopted wind parameters. At this time we expect the reverse shock to have a radius  $r_{\text{rs,life}} \approx 0.6 \text{ pc}$  (see Eq. 7), and for the bubble to still be overpressured with respect to the ambient medium by a factor of  $\approx 20$ . Our parameters also give  $r_{\text{inj,max}} = 2.68 \text{ pc}$ .

We use 10 grid cells for the injection region in all of our calculations. We do not expect our results to be very sensitive to the exact number of cells in this region, but a minimum of 4 is probably a good idea.

### 4.1 A model with ‘‘high’’ resolution

We begin by using the method in Sec. 3.1.1 to setup and continue blowing the wind; i.e. the momentum and energy within the 10 closest cells to the grid origin is overwritten after every step.

For our chosen parameters,  $t_{\text{eq}} = 1.2 \times 10^8 \text{ s}$  (3.8 yr). In this time a freely expanding wind will have blown out to a radius  $r_{\text{eq}} = v_w t_{\text{eq}} = 0.008 \text{ pc}$ . To satisfy the constraint that  $r_{\text{inj}} \ll r_{\text{eq}}$ , we use a grid with 1200 cells, with an initial uniform cell width  $dr_0 = 10^{-5} \text{ pc}$ . The wind initially extends out to the edge of the injection region ( $r_{\text{inj}} = 10^{-4} \text{ pc}$ ). The flow time of the wind to this radius is  $t = 1.54 \times 10^6 \text{ s}$ , which is  $\ll t_{\text{eq}}$ , as required.

The average wind density in the last cell in the injection region is initially  $2.9 \times 10^{-20} \text{ g cm}^{-3}$ , which is more than 10 times the density of the ambient gas. The impact of the wind on the ambient gas creates two shocks, which in this case both move outwards on the grid (with a density below  $\approx 2.2 \times 10^{-23} \text{ g cm}^{-3}$  in the final cell in the injection region the reverse shock initially moves towards the grid origin and into the injection region - it is vital that this is avoided otherwise some mass, momentum and energy is lost from the simulation).

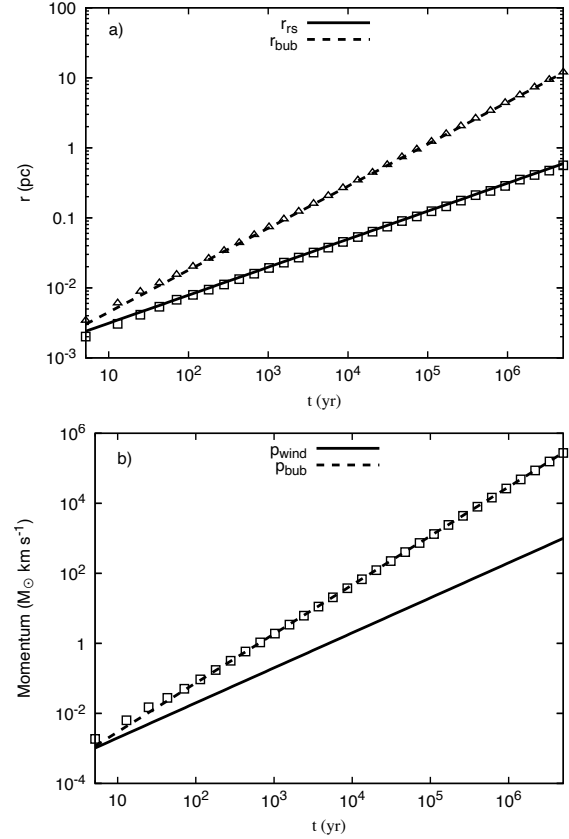


**Figure 1.** a) The radii of the reverse shock and forward shock, and b) the momentum of the bubble, as a function of bubble age. Data from model *modx* is shown by the points, while the lines show the analytical values for the shock positions (Eqs. 4 and 1) and for the integrated wind and bubble momenta (Eqs. 8 and 9).

We fix the size of the grid for a time  $t_{\text{fix}} = (r_{\text{max},0} - r_{\text{inj}})/v_w$ , where the maximum grid radius is initially  $r_{\text{max},0} = 1.2 \times 10^{-2} \text{ pc}$ . After this time we make the grid expand at a rate such that  $r_{\text{max}} = r_{\text{max},0} (t/t_{\text{fix}})^{3/5}$ . As the grid expands, so does the injection region. This has no effect on the results provided that the reverse shock remains outside of the injection region, and we can confirm that this constraint is satisfied at all times. We set the time at the start of the simulation to  $t = 0$ . After 5 Myr of evolution, the grid has expanded to the extent that  $dr = 0.36 \text{ pc}$  and  $r_{\text{max}} = 43.6 \text{ pc}$ . We refer to this model as ‘‘modx’’ (‘‘x’’ for ‘‘expansion’’) for the remainder of this paper, and we adopt it as our reference simulation.

The radii of the forward and reverse shocks as a function of time are shown in Fig. 1a). Both shocks move steadily outwards. They are reasonably close together when the bubble is young, but since the bubble expands faster than the reverse shock, most of the bubble becomes occupied by hot shocked stellar wind material at later times. The radii measured from the numerical simulation agree very well with the analytical expectations ( $r_{\text{rs}}$  and  $r_{\text{bub}}$ ).

The momentum of the bubble and the integrated injected momentum of the wind are shown in Fig. 1b). At very early times the momentum measured from the simulation is slightly above the expected value from the Weaver et al. (1977) model, but within 100 yrs the two obtain excellent agreement and then continue to do so. The bubble momentum reaches a maximum of  $2.76 \times 10^5 M_{\odot} \text{ km s}^{-1}$  at  $t = 5 \text{ Myr}$ , giving a momentum boost  $\beta = 276$ . The final momentum is within 2% of the value predicted by the Weaver et al. (1977)

model ( $2.81 \times 10^5 M_{\odot} \text{ km s}^{-1}$ ). This difference is due to the small amount of cooling that takes place in the shocked stellar wind in the simulation.

#### 4.2 The effect of numerical resolution

We now investigate how the bubble momentum changes if we change the numerical resolution of our simulation. We know that we will miss some of the momentum boost that the bubble provides if we do not satisfy  $t \ll t_{\text{eq}}$ , and we want to explore how this loss varies with  $\chi$ . To do so we run simulations with a fixed (non-expanding) grid. We begin with a resolution  $dr = 0.025$  pc. With the standard 10 cell injection region the edge of the injection region is at  $r_{\text{inj}} = 0.25$  pc, giving  $\chi = 0.093$ . This resolution should be just about high enough for the simulated bubble to match the analytical predictions reasonably well. We refer to this model as “*meo\_0.1*” (“*meo*” for the wind launch mechanism (momentum and energy overwrite) and “*0.1*” for the value of  $\chi$  used).

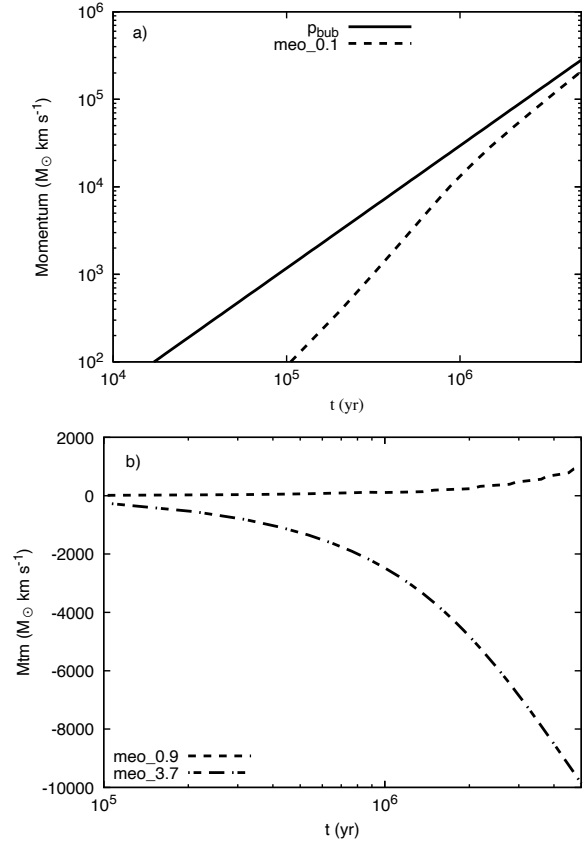
The flow time of the wind out to  $r_{\text{inj}}$  is about 120 years. The ram pressure of the wind at the edge of the injection region is  $\rho_w v_w^2|_{\text{inj}} = 1.8 \times 10^{-10} \text{ dyn cm}^{-2}$ , which is more than 100× higher than the thermal pressure of the ambient medium. Nevertheless, we find that the reverse shock initially tries to move back into the injection region, and since the cell variables are overwritten at each step this causes a small amount of mass and energy to be lost at early times (this loss is avoided with the other wind launch methods). The reverse shock eventually moves away from the injection region as the bubble grows and becomes established.

Fig. 2a) shows the bubble momentum from this simulation. Compared to model *modx* the radial momentum is significantly lower at early times as the bubble tries to establish itself. In addition, the momentum of the bubble never fully catches up to that in model *modx* or the analytical value, being still 25% lower after 5 Myrs.

The situation becomes much worse if the grid cell size is further increased. Fig. 2b) shows the bubble momentum from models *meo\_0.9* with  $dr = 0.25$  pc ( $r_{\text{inj}} = 2.5$  pc;  $\chi = 0.93$ ) and *meo\_3.7* with  $dr = 1.0$  pc ( $r_{\text{inj}} = 10$  pc;  $\chi = 3.73$ ). The ram pressures of the winds at the edge of the injection regions are now  $\rho_w v_w^2|_{\text{inj}} = 1.8 \times 10^{-12} \text{ dyn cm}^{-2}$  and  $1.0 \times 10^{-13} \text{ dyn cm}^{-2}$ , respectively. The former marginally exceeds  $P_{\text{amb}}$ , which allows for a small amount of hot gas to be created just outside of the injection region (see Fig. 3). However, although formally  $r_{\text{inj}} < r_{\text{inj,max}}$ , the shocked gas is not able to do any useful  $PdV$  work and the final radial momentum of  $\approx 10^3 M_{\odot} \text{ km s}^{-1}$  is only equal to the momentum injected by the wind ( $\beta \approx 1.0$ ). The bubble is not able to grow outside of the injection region (and finished with a smaller radius than in model *modx*), and nearly all of the surrounding medium remains undisturbed.

For model *meo\_3.7* with  $dr = 1.0$  pc the circumstances are even worse. Since  $r_{\text{inj}} > r_{\text{inj,max}}$ , the bubble is completely quenched by the ambient pressure outside of the injection region. This results in an inflow developing with negative radial momentum (see Fig. 2b), in complete disagreement with the higher resolution models and analytical expectations.

Density, pressure and temperature profiles from the simulations at  $t = 5$  Myr are shown in Fig. 3. Model *modx* is our high resolution reference, and has radii  $r_{\text{rs}} \approx 0.53$  pc,  $r_{\text{cd}} \approx 11.7$  pc, and  $r_{\text{bub}} \approx 11.9$  pc. In model *meo\_0.1*, the reverse shock position and the shocked wind density, pressure and temperature all agree with model *modx*. However, the shocked gas does not extend as far out from the star, resulting in the contact discontinuity, swept-up shell,



**Figure 2.** The momentum of the bubble as a function of bubble age for simulations with various fixed resolutions. a)  $dr = 0.025$  pc (model *meo\_0.1*; dashed line). Also shown is the Weaver et al. (1977) analytical prediction, which model *modx* nearly approaches. b)  $dr = 0.25$  pc (model *meo\_0.9*; dashed line) and  $dr = 1$  pc (model *meo\_3.7*; dot-dashed line).

and forward shock all appearing at too small radii ( $r_{\text{cd}} \approx 10.5$  pc and  $r_{\text{bub}} \approx 10.8$  pc).

In model *meo\_0.9* the unshocked wind is forced to extend too far from the star (past the position of the reverse shock in the reference model). The smaller ram pressure at the edge of the injection region is unable to grow a bubble and no significant hot gas is created (only a small and narrow temperature spike at the edge of the injection region - see Fig. 3b). In model *meo\_3.7* the unshocked wind is forced to extend out to a radius of 10 pc, leading to a wind density of  $2.7 \times 10^{-30} \text{ g cm}^{-3}$  at the edge of the injection region. This produces a ram pressure below  $P_{\text{amb}}$ , and backflow of gas.

#### 4.3 Other injection mechanisms

In the previous subsection we examined the resolution dependence of models with a momentum and energy overwrite (as in Sec. 3.1.1), which have a prefix of “*meo*”.

We now examine models with energy injection (Sec. 3.1.2), which have a prefix of “*ei*”, and models with momentum and energy injection (Sec. 3.1.3) which have a prefix of “*mei*”. We explore the same 3 values of  $\chi$  as before, with models identified with the same “*0.1*”, “*0.9*” or “*3.7*” postfix. We have also confirmed that when we use an expanding grid, with  $dr_0 = 10^{-5}$  pc, different wind setups produce identical bubbles with identical momenta (the momenta are within 0.1% at  $t = 5$  Myr).

Note that we find that when an “injection” method (either *ei* or

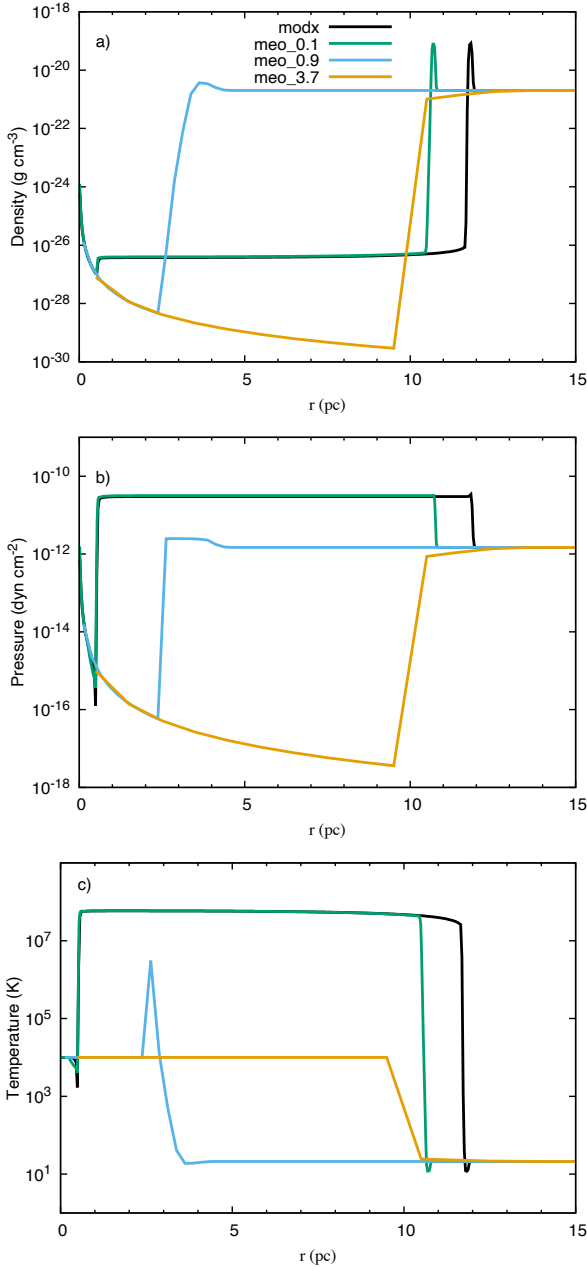


**Figure 3.** Profiles of a) density; b) pressure; c) temperature at  $t = 5$  Myr for models *modx*, *meo\_0.1*, *meo\_0.9* and *meo\_3.7*. The ambient density, pressure and temperature values are visible on the far right of each plot. Models with  $\chi = 0.1, 0.9$  and  $3.7$  have  $r_{\text{inj}} = 0.25$  pc,  $2.5$  pc and  $10$  pc, respectively. Note the differences in the positions of the reverse shock, contact discontinuity, and shell, and the amount of hot gas, as the resolution is varied.

*mei*) is used, in models with poor resolution (postfix *0.9* or *3.7*), the nature of the resulting bubble is dependent on whether additional constraints are placed on the courant number and timestep. Bubbles are slightly more “successful” in these scenarios if the initial courant number is set very low (e.g.,  $< 10^{-4}$ ) and slowly increased as the simulation progresses, and also if the global timestep is in addition limited by the minimum net cooling time of the gas in any cell. Models *ei\_0.9*, *ei\_3.7*, *mei\_0.9* and *mei\_3.7* all have these additional constraints.

Fig. 4a) shows the bubble momentum from simulations with a

**Table 1.** The models investigated. The columns show the model name, the wind launch method (see Sec. 3.1), the radius of the injection region, the ratio of the injection region radius to its maximum possible value (Eq. 15), and the momentum of the bubble and boost factor after 5 Myr. Model *modx* is the reference simulation that closely matches the analytical solution. All of the different wind launch methods result in exactly the same bubble properties in model *modx*, although in this paper we report on only the *meo* version. The maximum size that the injection region can be before any bubble is completely quenched is  $r_{\text{inj,max}} = 2.68$  pc (Eq. 14), corresponding to  $\chi = 1.0$ .

Model	Launch Method	$r_{\text{inj}}$ (pc)	$\chi$	$p_{\text{bub}}$ ( $M_{\odot} \text{ km s}^{-1}$ )	$\beta$
<i>modx</i>	<i>meo</i>	$10^{-4}$	$3.73 \times 10^{-5}$	$2.76 \times 10^5$	276
<i>meo_0.1</i>	<i>meo</i>	0.25	0.093	$2.09 \times 10^5$	209
<i>meo_0.9</i>	<i>meo</i>	2.5	0.93	966	0.97
<i>meo_3.7</i>	<i>meo</i>	10	3.73	-9860	-9.9
<i>ei_0.1</i>	<i>ei</i>	0.25	0.093	$2.22 \times 10^5$	222
<i>ei_0.9</i>	<i>ei</i>	2.5	0.93	523	0.52
<i>ei_3.7</i>	<i>ei</i>	10	3.73	151	0.15
<i>mei_0.1</i>	<i>mei</i>	0.25	0.093	$2.23 \times 10^5$	223
<i>mei_0.9</i>	<i>mei</i>	2.5	0.93	$5.30 \times 10^4$	53
<i>mei_3.7</i>	<i>mei</i>	10	3.73	708	0.71

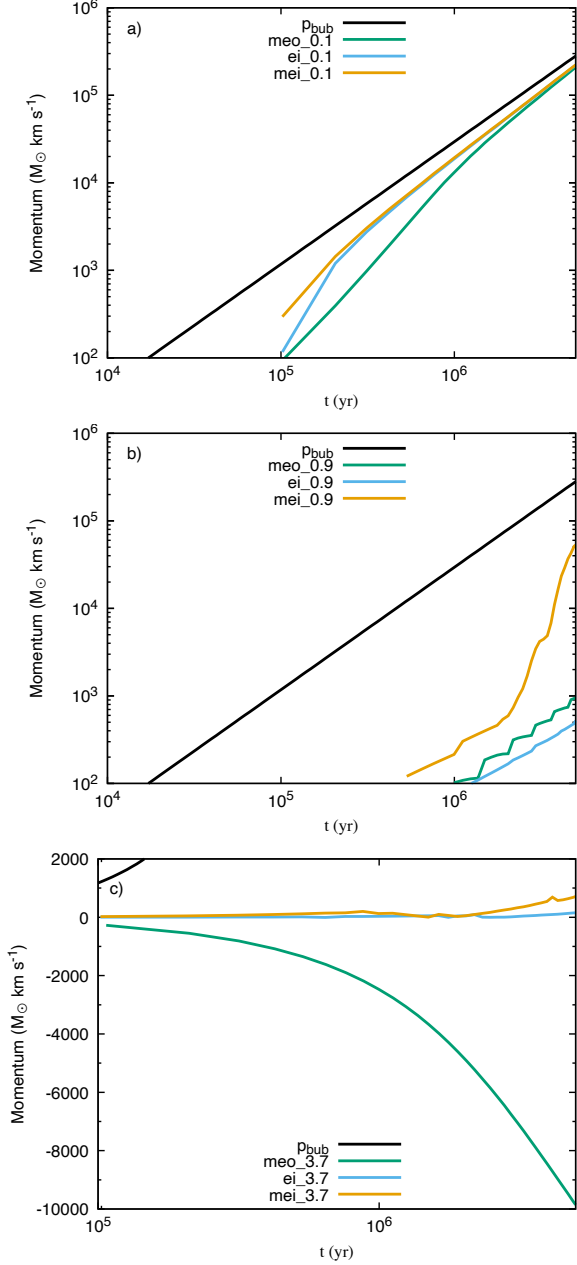
fixed  $dr = 0.025$  pc ( $\chi = 0.093$ ) and different wind injection mechanisms. We see that the momentum rises most quickly for method *mei*, then *ei*, and slowest for method *meo*. The final momentum produced for method *meo* is also about 6% lower than obtained for methods *ei* and *mei*. This behaviour is likely due to the reverse shock initially interacting with the injection region in method *meo*, and results in a slightly smaller bubble as shown in Fig. 5a) which shows the corresponding temperature profiles. All 3 methods produce final momenta which are 20% lower (and bubbles that are slightly smaller) than obtained for our reference model (*modx*).

Fig. 4b) shows the bubble momentum from simulations with a fixed  $dr = 0.25$  pc ( $\chi = 0.93$ ). Fig. 5b) shows the corresponding temperature profiles. We see that methods *meo* and *ei* are not able to generate a hot bubble. However, method *mei* is more successful in this regard, and though the hot gas only extends out to  $\approx 5$  pc (instead of the  $\approx 12$  pc seen in the reference simulation *modx*), it is able to do significant  $PdV$  work, producing a final bubble momentum which is within a factor of 10 of the analytical value (this is not the case if the additional restrictions of an initially smaller courant number and timesteps limited by the net cooling time are not implemented).

Fig. 4c) shows the bubble momentum from simulations with a fixed  $dr = 1$  pc ( $\chi = 3.73$ ). Fig. 5c) shows the corresponding temperature profiles. No hot gas is generated using any of the methods. With method *mei* the momentum of the gas ( $700 M_{\odot} \text{ km s}^{-1}$ ) is less than the injected wind momentum ( $10^3 M_{\odot} \text{ km s}^{-1}$ ), while method *ei* results in only  $150 M_{\odot} \text{ km s}^{-1}$  of momentum.

In Table 2 and Fig. 6 we show the bubble momentum, normalized to that from *modx*, as a function of the ratio  $\chi = r_{\text{inj}}/r_{\text{inj,max}}$ . We see that all 3 methods capture 75 – 80% of the expected bubble momentum when  $\chi = 0.1$ . This value of  $\chi$  marks a turning point for the bubble momentum when using method *meo*, which displays a power-law decline between  $\chi = 0.2 - 0.8$ . Less than 1 per cent of the expected bubble momentum is attained when  $\chi = 0.8$ . In contrast, with methods *mei* and *ei* the bubble momentum remains closer to the reference model when  $\chi > 0.1$ , although a sharp decline eventually occurs. Method *mei* is still able to create a hot bubble when  $\chi = 1.0$ , though this ability disappears for values of  $\chi \gtrsim 1.0$ .

Fig. 6 shows that we must have  $\chi \lesssim 0.1$  in order to obtain a bubble



**Figure 4.** The momentum of the bubble as a function of bubble age for simulations with a fixed grid and different wind injection mechanisms. a)  $dr = 0.025$  pc ( $\chi = 0.093$ ); b)  $dr = 0.25$  pc ( $\chi = 0.93$ ); c)  $dr = 1$  pc ( $\chi = 3.73$ ). Also shown is the [Weaver et al. \(1977\)](#) analytical prediction.

momentum within 20 – 25% of the analytical (or reference model) value. To be within 10% of the analytical value requires  $\chi \lesssim 0.02$ .

## 5 DISCUSSION

In Sec. 4 we find that the momentum of the bubble can be significantly underestimated in simulations where the numerical resolution is insufficient. For a bubble to be created we require  $\chi = r_{\text{inj}}/r_{\text{inj,max}} < 1$ . However, for a bubble to match the analytical solution reasonably well requires  $\chi < 0.1$ , and still higher resolutions are required to obtain a momentum boost within 10 per cent of the analytical solution.

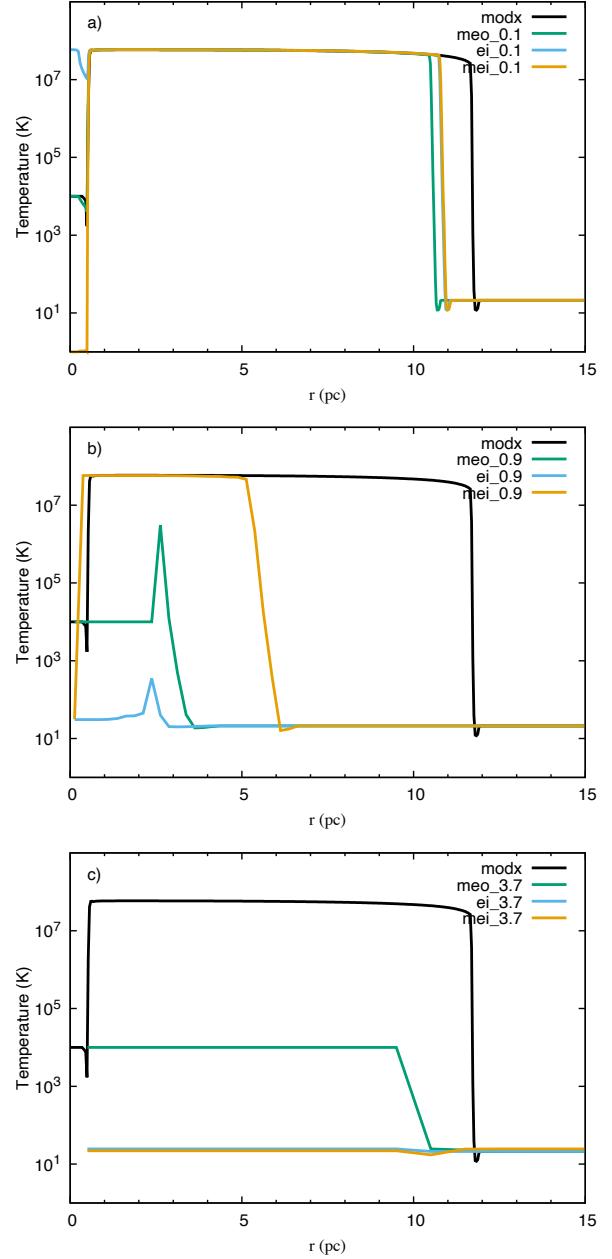


**Figure 5.** Temperature profiles for simulations with different wind injection mechanisms and a fixed grid. a)  $dr = 0.025$  pc ( $\chi = 0.093$ ); b)  $dr = 0.25$  pc ( $\chi = 0.93$ ); c)  $dr = 1$  pc ( $\chi = 3.73$ ). Also shown is the temperature profile from model *modx*.

In the literature, simulations with a variety of values for  $\chi$  can be found. In their stellar feedback paper, [Rogers & Pittard \(2013\)](#) used a resolution  $dx = 0.0625$  pc, and an injection region radius  $r_{\text{inj}} = 6 dx = 0.375$  pc. For the first 4 Myr of the simulation, the wind momentum injection rate was  $\dot{p}_{\text{wind}} = 1.14 \times 10^{28}$  g cm s<sup>-2</sup>. The average ambient pressure within the GMC clump that the stellar feedback blows into was  $2.8 \times 10^{-13}$  dyn cm<sup>-2</sup>. This gives  $r_{\text{inj,max}} = 18.5$  pc and  $\chi \approx 0.02$ . Therefore, the bubble that forms is initially highly overpressured and has no problem in growing. We expect that nearly all of the initial growth in the bubble momentum will have been captured (although at later times the bubble expands off the grid).

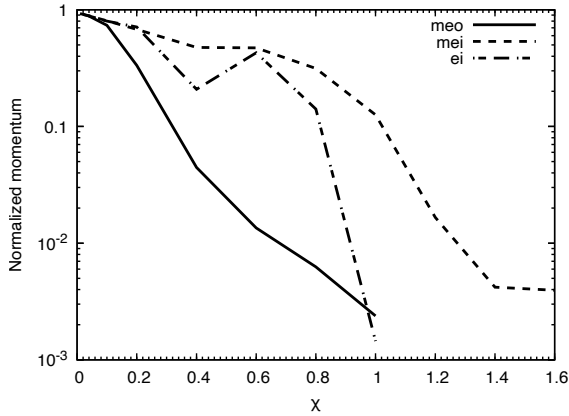


**Figure 6.** The bubble momentum normalized to that from the reference model *modx*, as a function of  $\chi$ , the ratio of the injection radius,  $r_{\text{inj}}$ , to the maximum injection radius,  $r_{\text{inj,max}}$ . Results for the three different wind launch methods are shown. The momenta are all measured at a bubble age of 5 Myr.

**Table 2.** The radial momentum of the bubble, as a function of  $\chi$ , for the 3 wind launch models investigated. The radial momentum has been normalized by the value from the high resolution reference model (*modx*). The momentum is measured at  $t = 5$  Myr.

$\chi$	<i>meo</i>	<i>ei</i>	<i>mei</i>
0.01	0.928	0.928	0.928
0.02	0.913	0.913	0.914
0.04	0.882	0.886	0.888
0.10	0.736	0.799	0.804
0.20	0.334	0.711	0.680
0.40	0.0446	0.208	0.475
0.60	0.0135	0.428	0.472
0.80	0.0063	0.141	0.314
1.00	0.0028	0.0015	0.126

An example where the wind injection has not been sufficiently resolved is [Geen et al. \(2015\)](#). In this paper feedback from a single  $15 M_{\odot}$  star into a variety of ambient densities and temperatures, spanning the range ( $n = 0.1 \text{ cm}^{-3}$ ,  $T = 62 \text{ K}$ ) to ( $n = 100 \text{ cm}^{-3}$ ,  $T = 8.2 \text{ K}$ ), is considered. The wind and the ionizing radiation from the star are both considered and it is concluded that the stellar wind has negligible impact. We estimate the wind parameters as  $\dot{M} \approx 10^{-8} M_{\odot} \text{ yr}^{-1}$  and  $v_w \approx 1000 \text{ km s}^{-1}$  (for solar abundances). For their densest ambient medium we estimate  $r_{\text{inj,max}} \approx 3 \text{ pc}$ , while for their lowest density medium we estimate  $r_{\text{inj,max}} \approx 35 \text{ pc}$ . As they use  $r_{\text{inj}} = 12 \text{ pc}$ , they either fail to launch a bubble at all ( $\chi \approx 4$ ), or the bubble expansion is severely compromised ( $\chi \approx 0.34$ ). Therefore, their claim that the stellar wind has negligible impact (see their Fig. 11) should be revisited.

[Haid et al. \(2018\)](#) study feedback into initially warm and ionized gas (WIM;  $\rho = 2.1 \times 10^{-25} \text{ g cm}^{-3}$  and  $T = 10^4 \text{ K}$ ) and into cold, predominantly neutral gas (CNM;  $\rho = 2.1 \times 10^{-22} \text{ g cm}^{-3}$  and  $T = 20 \text{ K}$ ). Both their WIM and CNM have  $P/k = 10^3 \text{ K cm}^{-3}$  and an injection radius of  $2.4 \text{ pc}$  is used. We estimate that  $r_{\text{inj,max}} = 1.8$ ,  $13$  and  $52 \text{ pc}$  for their models with stars of mass  $M_* = 12$ ,  $23$  and  $60 M_{\odot}$ , respectively, giving  $\chi \approx 1.3$ ,  $0.18$  and  $0.05$ . Thus we expect the bubble around their  $12 M_{\odot}$  star to be completely missing, and it should be significantly compromised around their  $23 M_{\odot}$  star. We believe that only their  $60 M_{\odot}$  star models blow a bubble that would

closely match higher resolution models. Our expectations appear to be valid: their Fig. 3 shows no evidence of hot gas in their  $12 M_{\odot}$  CNM model, while their Figs. 3 and 5 reveal the presence of a reverse shock only for the  $23$  and  $60 M_{\odot}$  models in the WIM, and for the  $60 M_{\odot}$  model in the CNM. Thus, the authors claims should also be reexamined.

Our own work is also not immune from these issues. Although the simulations with the  $40 - 120 M_{\odot}$  stars in [Wareing et al. \(2017a,b\)](#) have  $\chi \lesssim 0.1$  and vigorously inflate bubbles, the wind injection in the  $15 M_{\odot}$  star simulations is estimated to have  $\chi \approx 0.5 - 0.6$ . Although hot ( $\sim 10^8 \text{ K}$ ) shocked stellar wind gas is present, and flows some distance from the injection region, a strong reverse shock is not always visible. Thus, the stellar wind impact is likely to be strongly underestimated in the  $15 M_{\odot}$  star simulations.

We would like to stress that the papers discussed in this section are simply ones that we are familiar with in the literature - there are likely to be other papers with similar issues. It also remains the case that even if the feedback from lower mass (e.g.,  $12 - 15 M_{\odot}$ ) stars has not always been modelled with sufficient resolution, the winds from such stars may still be too weak to strongly affect their environment. If this is so, the conclusions from these papers will still stand.

Our results are presented for a uniform medium and show that the ram and/or thermal pressure at the edge of the injection region must significantly exceed the ambient pressure in order to correctly inflate the bubble. In reality, bubbles usually interact with a highly inhomogeneous medium. Previous work in the literature (e.g., [Rogers & Pittard 2013](#); [Kim, Ostriker & Raileanu 2017](#); [Lancaster et al. 2021b](#)) shows that the size and structure of the bubble depends on the number, size, density contrast and distribution of the clouds. The location of the reverse shock may in places be determined by the position of individual clouds. However, since  $r_{\text{inj,max}}$  depends on  $P_{\text{amb}}$  (not  $\rho_{\text{amb}}$ ), the requirement that  $\chi$  needs to be significantly less than unity likely remains valid.

We note two further points. While we have only focussed on the thermal pressure of the surroundings, the position of the reverse shock will in fact depend on the *total* pressure (thermal + magnetic + turbulent + cosmic ray). When there is significant non-thermal pressure, the total ambient pressure should be used when evaluating  $r_{\text{inj,max}}$ . Finally, if one is only concerned with momentum-driven feedback no constraint exists on the value of  $\chi$ . This is because no extra momentum is being created through  $PdV$  work by a hot bubble. In such cases it should be possible to use very low numerical resolution (though this has other consequences, such as the ability to resolve structures and flows at a particular scale).

## 6 SUMMARY AND CONCLUSIONS

We have examined the numerical resolution requirements to blow energy-driven stellar wind bubbles in a uniform medium. We have determined a maximum radius for the wind injection region,  $r_{\text{inj,max}}$ , above which a bubble will not usually grow. This applies to all 3 wind injection mechanisms studied. If  $\chi = r_{\text{inj}}/r_{\text{inj,max}} < 1$  is only marginally satisfied, the resulting bubble will be only marginally overpressured and unable to generate the large momentum boost that it should.

In order for the bubble momentum to match analytical predictions, the very early growth of the bubble must be captured as accurately as possible which requires very high resolution. To ensure this, the flow time of the wind out to the edge of the injection region should be significantly less than the time at which the free-flowing wind and bubble momenta are equal ( $t_{\text{eq}}$ ). This requires that  $r_{\text{inj}} \ll t_{\text{eq}}/v_w$ .

If  $r_{\text{inj}}$  is appropriately chosen, the two-shocks that initially develop when using method *meo* should both move outwards. This ensures that no mass, momentum, or energy is lost from the simulation. All 3 injection methods yield the same bubble properties and momentum for such small values of  $r_{\text{inj}}$ .

As  $\chi$  is increased, the bubble loses more and more momentum, due to the absence of the high initial pressures that actual bubbles have. When  $0.1 < \chi \leq 1.0$  the momentum and energy (*mei*) wind injection method outperforms the other methods (restrictions on the courant number and radiative cooling limits on the timestep aside). However, if  $\chi = 0.1$ , we find that 20–25% of the bubble momentum is still missed. To be within 10% of the momentum from the reference model requires  $\chi \lesssim 0.02$ , in which case all wind injection methods perform similarly without the need for such additional restrictions.

This paper highlights that the injection region of the stellar wind must be adequately resolved. Because our calculations are one dimensional, restrict cooling at unresolved interfaces, and do not include thermal conduction or explicit mixing of hot and cold phases, the cooling of the hot gas inside the bubble is minimised (and the momentum of the bubble is maximised). The actual impact of these restrictions and processes is still to be determined.

## ACKNOWLEDGEMENTS

We thank the referee for their helpful comments. JMP was supported by grant ST/P00041X/1 (STFC, UK).

## DATA AVAILABILITY

The data underlying this article are available in the Research Data Leeds Repository, at <https://doi.org/10.5518/1046>.

## REFERENCES

- Chevalier R. A., Clegg A. W., 1985, *Nature*, 317, 44  
 Chevanche M., et al., 2020, *MNRAS*, 493, 2872  
 Chevanche M., et al., 2021, *MNRAS*, submitted (arXiv:2010.13788)  
 Dale J. E., Ngoumou J., Ercolano B., Bonnell I. A., 2014, *MNRAS*, 442, 694  
 Dinnbier F., Walch S., 2020, *MNRAS*, 499, 748  
 Dyson J. E., Williams D. A., 1980, *The Physics of the Interstellar Medium*. Halsted Press, New York  
 El-Badry K., Ostriker E. C., Kim C.-G., Quataert E., Weisz D. R., 2019, *MNRAS*, 490, 1961  
 García-Segura G., Franco J., 1996, *ApJ*, 469, 171  
 Gatto A., et al., 2017, *MNRAS*, 466, 1903  
 Geen S., Rosdahl J., Blaizot J., Devriendt J., Slyz A., 2015, *MNRAS*, 448, 3248  
 Geen S., Bieri R., Rosdahl J., de Koter A., 2021, *MNRAS* (arXiv:2009.08742)  
 Girichidis P., Seifried D., Naab T., Peters T., Walch S., Wunsch R., Glover S. C. O., Klessen R. S., 2018, *MNRAS*, 480, 3511  
 Gnat O., Ferland G. J., 2012, *ApJS*, 199, 20  
 Grevesse N., Asplund M., Sauval A. J., Scott P., 2010, *Ap&SS*, 328, 179  
 Haid S., Walch S., Seifried D., Wunsch R., Dinnbier F., Naab T., 2018, *MNRAS*, 478, 4799  
 Kaastra J. S., 1992, *An X-ray Spectral Code for Optically Thin Plasmas*. Internal SRON-Leiden Report  
 Kim C.-G., Ostriker E. C., Raileanu R., 2017, *ApJ*, 834, 25  
 Koyama H., Inutsuka S.-I., 2000, *ApJ*, 532, 980  
 Kruijssen J. M. D., et al., 2019, *Nature*, 569, 519  
 Krumholz M. R., Stone J. M., Gardiner T. A., 2007, *ApJ*, 671, 518  
 Lancaster L., Ostriker E. C., Kim J.-G., Kim C.-G., 2021, *ApJ*, 914, 89  
 Lancaster L., Ostriker E. C., Kim J.-G., Kim C.-G., 2021, *ApJ*, 914, 90

- Mewe R., Kaastra J. S., Liedahl D. A., 1995, *Legacy*, 6, 16  
 Peters T., et al., 2017, *MNRAS*, 466, 3293  
 Pittard J. M., 2013, *MNRAS*, 435, 3600  
 Rathjen T.-E., Naab T., Girichidis P., Walch S., Wunsch R., Dinnbier F., Seifried D., Klessen R. S., Glover S. C. O., 2021, *MNRAS*, 504, 1039  
 Rogers H., Pittard J. M., 2013, *MNRAS*, 431, 1337  
 Shetty R., Ostriker E. C., 2012, *ApJ*, 754, 2  
 Smith M. C., Sijacki D., Shen S., 2019, *MNRAS*, 485, 3317  
 Sutherland R. S., 2010, *Ap&SS*, 327, 173  
 Wareing C. J., Pittard J. M., Falle S. A. E. G., Van Loo S., 2016, *MNRAS*, 459, 1803  
 Wareing C. J., Pittard J. M., Falle S. A. E. G., 2017a, *MNRAS*, 465, 2757  
 Wareing C. J., Pittard J. M., Falle S. A. E. G., 2017b, *MNRAS*, 470, 2283  
 Wareing C. J., Pittard J. M., Wright N. J., Falle S. A. E. G., 2018, *MNRAS*, 475, 3598  
 Weaver R., McCray R., Castor J., Shapiro P., Moore R., 1977, *ApJ*, 218, 377  
 Wunsch R., Tenorio-Tagle G., Palouš J., Silich S., 2008, *ApJ*, 683, 683

This paper has been typeset from a  $\text{\TeX}/\text{\LaTeX}$  file prepared by the author.